Spatial Variability of Relative Sea-Level Rise in Tianjin, China: Insight From InSAR, GPS, and Tide-Gauge Observations

Wei Tang, Wei Zhan, Bowen Jin, Mahdi Motagh, and Yubin Xu

***Abstract*—The Tianjin coastal region in Bohai Bay, Northern China, is increasingly affected by storm-surge flooding which is exacerbated by anthropogenic land subsidence and global sea-level rise (SLR). We use a combination of synthetic aperture radar interferometry (InSAR), continuous GPS (CGPS), and tide-gauge observations to evaluate the spatial variability of relative SLR (RSLR) along the coastline of Tianjin. Land motion obtained by integration of 2 tracks of Sentinel-1 SAR images and 19 CGPS stations shows that the recent land subsidence in Tianjin downtown is less than 8 mm/yr, which has significantly decreased with respect to the last 50 years (up to 110 mm/yr in the 1980s). This might benefit from the South-to-North Water Transfer Project which has provided more than 1.8 billion cubic meters of water for Tianjin city since 2014 and reduced groundwater consumption. However, subsidence centers have shifted to suburbs, especially along the coastline dominated by reclaimed harbors and aquaculture industry, with localized subsidence up to 170 mm/yr. Combining InSAR observations with sea level records from tide-gauge stations reveals spatial variability of RSLR along the coastline. We find that, in the aquaculture zones along the coastline, the rates of land subsidence are as high as 82 mm/yr due to groundwater extraction for fisheries, which subsequently cause local sea levels to rise nearly 30 times faster than the global average. New insights into land subsidence and local SLR could help the country's regulators to make decisions on ensuring the sustainable development of the coastal aquaculture industry.**

***Index Terms*—Coastal aquaculture industry, coastal land subsidence, synthetic aperture radar interferometry (InSAR), sea-level rise (SLR), Tianjin coastal region.**

Manuscript received September 18, 2020; revised November 27, 2020 and January 1, 2021; accepted January 13, 2021. Date of publication January 26, 2021; date of current version March 3, 2021. This work was supported in part by the National Key R&D Program of China under Grant 2018YFC1503606 and Grant 2018YFC1508602, in part by the Natural Science Foundation of China under Grant 42001368, and the Fundamental Research Funds for the Central Universities under Grant 2020YQDC06. The work of Wei Zhan was supported by China Scholar Council, Hokkaido University. *(Corresponding author: Wei Zhan.)*

Wei Tang is with the College of Geoscience and Surveying Engineering, China University of Mining and Technology, Beijing 100083, China (e-mail: weitang@cumtb.edu.cn).

Wei Zhan is with the First Monitoring and Application Center, China Earthquake Administration, Tianjin 300180, China (e-mail: zw000373@163.com).

Bowen Jin is with the National Marine Data and Information Service, Ministry of Natural Resources, Tianjin 300171, China (e-mail: jbwnmdis@126.com).

Mahdi Motagh is with the GFZ German Research Centre for Geosciences, Department of Geodesy, Section of Remote Sensing and Geoinformatics, 14473 Potsdam, Germany, and also with the Institute of Photogrammetry and Geoinformation, Leibniz University Hannover, 30167 Hannover, Germany (e-mail: motagh@gfz-potsdam.de).

Yubin Xu is with the China Academy of Civil Aviation Science and Technology, Beijing 100028, China (e-mail: xuyubin0450@163.com).

This article has supplementary downloadable material available at https://doi.org/10.1109/JSTARS.2021.3054395, provided by the authors.

Digital Object Identifier 10.1109/JSTARS.2021.3054395

I. Introduction

TIANJIN is a coastal city in Northern China on the shore of Bohai Sea (see Fig. 1). The coastal region has an elevation generally below the mean sea level (down to −4 m m.s.l) and never exceeds 2 m above m.s.l. Due to the low surface elevation, land and sea level are in a delicate balance. This makes the Tianjin coastal region more sensitive to environmental changes including, but not limited to, land subsidence, sea level rise (SLR) [1], coastal erosion [2], saltwater intrusion [3], and salinification of soil and water [4], [5]. Among them, land subsidence had caused great adverse effects to the entire coastal region in Tianjin, with subsiding rates up to 110 mm/yr over the past 50 years [6]. Over-pumping of groundwater was the leading driving reasons for the land subsidence. This was revealed from the geodetic and hydrological measurements that the groundwater storage in the North China Plain (NCP) depleted at a rate of 1.7 ± 0.1 cm/yr from 2004 to mid-2016 and accelerated to 3.8 ± 0.1 cm/yr from mid-2013 to mid-2016 [7]. Long-term groundwater depletion has also been observed from spaceborne gravity measurements—gravity recovery and climate experiment in the NCP [8]–[10], which shows a good correlation between the land subsidence and groundwater abstraction [11]. The subsiding rates have significantly decreased in recent years because local government has tightened groundwater management to cope with this geological problem [12]. Particularly, the groundwater consumption was largely reduced since the South-to-North Water Transfer Project (SNWTP) put into operation in December 2014. Now, the water supply of residents in 14 districts of Tianjin is all from this water diversion project. Fig. 1 shows recent ground subsidence rates from continuous GPS (CGPS) between 2016 and 2019, displaying that most areas subsiding at rates less than 30 mm/yr. However, land subsidence is still a process threatening this city, especially along the coastal region dominated by aquaculture industry where groundwater is still extensively pumping for aquafarms.

Land subsidence exacerbates the relative SLR (RSLR) in the coastal regions around the world, such as Hampton Roads, USA [14], [15], Jakarta, Indonesia [16], [17], Mekong Delta, Vietnam [18], [19], Shanghai, China [20], [21] and Tianjin, China [1],

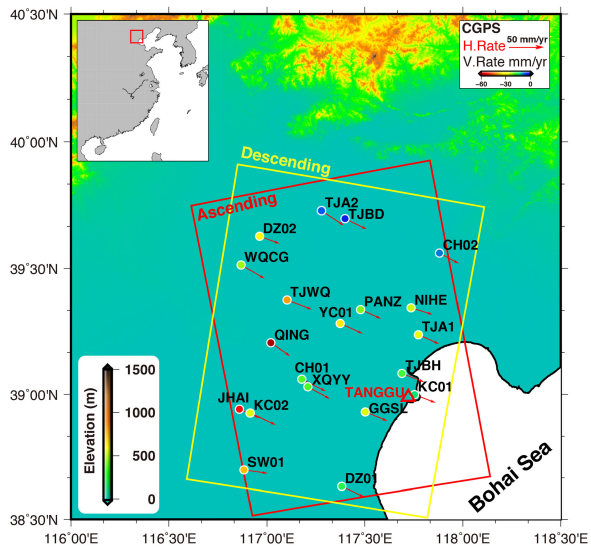

Fig. 1. Overview of the study area showing the frames of InSAR swath and CGPS stations (circles) used in our analysis. The color-coded circles represent the CGPS vertical displacement rates. The red arrows indicate the CGPS horizontal displacements with respect to the ITRF 2008 reference frame. CGPS data were acquired from 2016–2019. The red triangle indicates the TANGGU tide-gauge station. The background: 30-m resolution of digital elevation model (DEM) from Shuttle Radar Topography Mission (SRTM) [13].

[22], [23]. In Tianjin coastal region, the situation is more severe. The average rate of the RSLR at TANGGU tide-gauge station (found the location in Fig. 1) was only 1.77 mm/yr between 1910–1937 when groundwater had not been exploited [24]. The land subsidence reached to a critical rate as high as 110 mm/yr when the groundwater extraction reached a maximum of 1200 million m^3 in 1980s [6]. This pumping-induced subsidence magnified the rate of RSLR at TANGGU to 24–48 mm/yr in the period of 1959–1985 [24]. Even though practices have been adopted to limit groundwater pumping and land subsidence rates have decreased, the current rate of RSLR is still greater than 25 mm/yr once the effect of land subsidence is taken into account [23].

The combined effects of land subsidence and rising sea level increase the susceptibility of coastal areas to storm surges and flooding [25]. A numerical simulation by taking local land subsidence into account demonstrated that even for the case of a low scenario (0.5 m of SLR in 2030), the current seawall will not be able to withstand a 1-in-100-years storm surge in Tianjin–Hebei coastal region [23]. Furthermore, Tianjin experienced rapid coastline changes due to large-scale anthropogenic land reclamation projects for economic growth. The rapid coastline development caused significant changes in the tidal dynamics of the Bohai Sea that the M2 tidal amplitudes have changed with up to 20 cm over the last three decades [26]. The increasing tides made the coastal region more sensitive to SLR [27]–[29]. The settlement of loose clay on the newly reclaimed lands further increase the RSLR. Accurate rate of land subsidence therefore is a critical information to produce accurate projections of future SLR.

Land subsidence at a spatially varying rates of 20–110 mm/yr since the 1950s have been measured and documented in Tianjin [6], [24], [30]. The latest comprehensive studies, including complementary data collected with synthetic aperture radar (SAR) images from ENVISAT and ALOS satellites, spirit leveling and precipitation data, showed a maximum rate of 170 mm/yr located in the west of Tianjin city [31]. High spatial resolution TerraSAR-X images from 2009 to 2013 were processed to depict a more detailed location of land subsidence [32]–[34]. Results from different datasets are consistent in spatial patterns and magnitude of subsidence rates. However, previous studies mainly focused on the inland urban areas of Tianjin while subsidence rates in nonurban, near-shore areas remain unknown. Over the past decades, the near-shore areas have been largely expanded by aquacultures to meet a growing demand for seafood consumption. Groundwater consumption by coastal aquacultures can contribute to land subsidence and consequently cause RSLR much faster than the global average [35]. Both land subsidence and sea level records are required to evaluate the spatial extent of RSLR and thus to make coastal management policies. However, only one tide-gauge station (TANGGU station shown in Fig. 1) is located in this region, which is not enough for the assessment of the RSLR in the entire coastal area because the rates of land subsidence vary with location. This emphasizes the need for the high-spatial resolution measurements of land subsidence provided by space-borne synthetic aperture radar interferometry (InSAR).

In this article, we used two complementary datasets: high spatial resolution of measurements from Sentinel-1 SAR images and high temporal resolution of daily CGPS observations to provide updated estimates of land subsidence in the year of 2017–2019 in Tianjin coastal region. Satellite SAR data were processed with a state-of-the-art time-series InSAR method and the main error source from atmosphere was carefully mitigated. The InSAR displacement measurements were then connected with the CGPS observations to generate deformation maps in a geodetic reference frame at a dense spatial resolution. Vertical land motion rates can be decomposed thanks to the available ascending and descending datasets from Sentinel-1 satellite. Finally, the high spatial resolution maps of land subsidence were combined with tide-gauge observations to examine the spatial variability of RSLR in the coastal region.

II. Data Analysis

A. CGPS Data Analysis

Nineteen CGPS stations located in our study area were used for analysis (see the locations of CGPS stations in Fig. 1). The raw data were processed using GAMIT/GLOBK 10.40 software [36] to obtain 3-D coordinates (north–south, east–west, and up–down) at each station with respect to the ITRF 2008 reference frame. The GPS coordinate changes were fitted by weighted linear squares with slope rate and annual and semiannual terms as [37]

$$y\ (t) = a + bt + \sum_{k\,=\,1}^{2} \left[S_k \sin\left(2\pi kt\right) + C_k \cos\left(2\pi kt\right)\right] + \varepsilon \tag{1}$$

TABLE I
SAR DATA USED IN THIS STUDY. N_{SAR} REPRESENTS THE NUMBER OF SAR IMAGES AND N_{Int} REPRESENTS THE NUMBER OF INTERFEROGRAMS

Satellite	Orbit direction	Path	Frame	N_{SAR}	N_{Int}	Time Period
Sentinel-1A	Ascending	69	124	72	226	20170103-20190410
Sentinel-1A	Descending	149	463	66	194	20170303-20190411

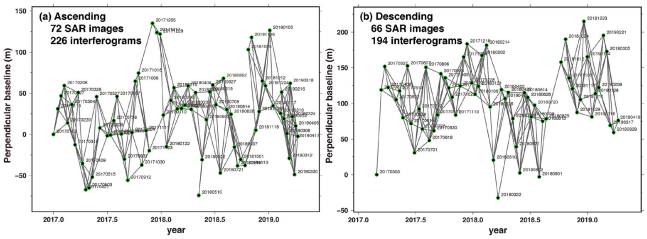

Fig. 2. Baseline-time plot of the Sentinel-1 ascending and descending data. The interferometric pairs were selected with a 100-m baseline threshold and 50-day temporal threshold.

with t the epoch in unit of year; a, b the intercept and linear rate; S_1, $C_1$the coefficients of annual components; and S_2, C_2 the coefficients of the semiannual components; ε the measurement errors. By using the trigonometric relations, the amplitudes (A_1, A_2) and phases $(\emptyset_1, \emptyset_2)$ of annual and semiannual components can be calculated as

$$A_k = \sqrt{{S_k}^2 + {C_k}^2},$$
$$\emptyset_k = \tan^{-1}\frac{C_k}{S_k}, \quad k = 1, 2. \tag{2}$$

B. InSAR Time Series Analysis

To investigate the recent land subsidence in Tianjin, we processed SAR images from Sentinel-1 satellite spanning the period from January 2017 to April 2019. Specifically, 72 images acquired from ascending track and 66 images acquired from descending track (see Table I) were used. We constructed 226 interferograms from the ascending scenes and 194 from the descending scenes (see Fig. 2), with a 50-day temporal threshold and a 100-m perpendicular baseline threshold. These interferograms were generated by the open source InSAR processing system GMT5SAR [38], [39]. SRTM 30m DEM [13] was used for the removal of topographic phase contribution. Phase unwrapping was performed by statistical-cost, network-flow algorithm for phase unwrapping (SNAPHU) [40] and implemented simultaneously on multiple processors by using the GNU Parallel to reduce processing time [41].

The coherence-based SBAS method [42], [43] was then adopted to extract the temporal evolution of ground deformation. The coherence information was incorporated into the least-square inverse problem as weights to suppress noises from low-coherence pixels. The weighted least-square inverse problem operated on each pixel can be expressed as

$$W\begin{bmatrix} 1 & 1 & 0 & \cdots & \beta B_{\perp,1} \\ 0 & 1 & 1 & \cdots & \beta B_{\perp,2} \\ \cdots & \cdots & \cdots & \cdots & \cdots \\ \frac{\rho}{\Delta t_1} & -\frac{\rho}{\Delta t_1} & 0 & \cdots & 0 \\ 0 & \frac{\rho}{\Delta t_2} & -\frac{\rho}{\Delta t_2} & \cdots & 0 \end{bmatrix}\begin{bmatrix} m_1 \\ m_2 \\ \cdots \\ m_j \\ h_{err} \end{bmatrix} = W\begin{bmatrix} d_1 \\ d_2 \\ \cdots \\ 0 \\ 0 \end{bmatrix} \tag{3}$$

where $W = diag\{\gamma_1, \gamma_2, \gamma_3, \cdots, \gamma_n\}$ is the weighting matrix with γ_i the coherence of the ith interferogram. $\beta = \frac{4\pi}{\lambda R \sin\theta}$ (λ the radar wavelength, R the range distance from the satellite to the center of the interferogram, θ the incidence angle), m_j is the incremental deformation for each SAR acquisition, d_i is the phase in the ith interferogram, h_{err} is the DEM error, ρ is the smoothing factor used to penalize unrealistically large temporal fluctuations. The design matrix has size of $[n \times s + 1]$, where n is the number of interferograms and s is the number of temporal incremental displacements. The time-series of cumulative line-of-sight (LOS) displacement was obtained by an iterative weighted least square method. The rate of deformation was then computed by linear regression on the displacement time series.

The accuracy of InSAR is severely limited by atmospheric delay, especially in the coastal region where a high content of atmospheric water vapor exists. The delays can be decomposed into a stratified and a turbulent component [44]. The stratified component is spatially correlated with topography and usually exhibit seasonal oscillations, however, the turbulent component is expected to be uncorrelated both spatially and temporally. In our study area, the stratified delay is expected to be small as the topography varies smoothly (see Fig. 1). We thus neglected the stratified delay and applied a common-point stacking approach to mitigate the turbulent delay. The basic idea of this method is that interferograms sharing a common acquisition have the same contribution from atmosphere [45]. The unwrapped phase $\Delta\emptyset$ can be written as

$$\Delta\emptyset_{ij} = \Delta\tau_{ij} + \alpha_j - \alpha_i + \epsilon_{ij} \tag{4}$$

where $\Delta\tau$ is the displacement signal, α is the atmospheric delay in each SAR scene (random in time), and ϵ represents random noise. By averaging of redundant interferograms that share a common scene, the delays can be estimated as follows:

$$\alpha_i = \lim_{N\to\infty}\frac{1}{2N}\sum_{j=1}^{N}\Delta\emptyset_{i(i-j)} - \Delta\emptyset_{(i+j)i} \tag{5}$$

where N is the number of SAR scenes.

We implemented the atmospheric mitigation method in combination with the above SBAS algorithm using an iterative procedure as described in [45] and the number of iterations is set to three. Fig. 3 shows examples of interferograms with significant improvement after atmospheric correction. The deformation maps are significantly contaminated by atmospheric delays [see Fig. 3(a) and (c)], especially in the near-coastal areas having abundant and rapidly time-varying water vapor content. As can be seen in Fig. 3, the atmospheric effects were significantly mitigated and the displacement signals were clearly observed after the corrections [see Fig. 3(b) and (d)].

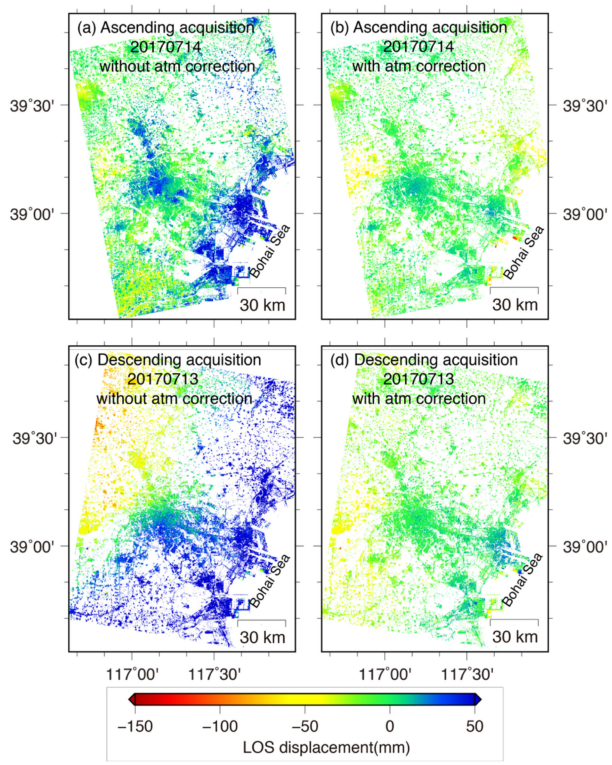

Fig. 3. Displacement maps acquired by SBAS method with and without atmospheric corrections. Significant error reduction can be found along the coastal area.

C. Datum Unification: Linking InSAR Measurements to Geodetic Reference Frame

The LOS deformation map derived from InSAR was combined with CGPS in order to tie the InSAR relative rates to the absolute CGPS geodetic reference frame. As a result of this procedure, both highly accurate and precise land subsidence maps at a dense spatial resolution can be generated for the purpose of computing RSLR in Tianjin coastal region. The procedure is as follows.

1) The 3-D coordinate changes resulting from CGPS analysis were first projected into the InSAR LOS vector as following [44]:

$$d_{LOS} = \begin{bmatrix} \sin\theta\sin\alpha & -\sin\theta\cos\alpha & \cos\theta \end{bmatrix} \begin{bmatrix} d_{North} \\ d_{East} \\ d_{Up} \end{bmatrix} \tag{6}$$

where α is the satellite heading angle (the satellite's orbit angle relative to true north), θ indicates the incidence angle (the angle between the local zenith and the radar wave).

2) A local reference frame was defined based on the two CGPS stations (TJA2 and TJBD) outside the region of expected subsidence, by subtracting the average of their coordinate changes from other CGPS sites. For InSAR processing, we also selected the two CGPS stations as the reference points by subtracting their average displacement value from other pixels. This step tied the InSAR relative measurements into the CGPS geodetic reference frame in space. Temporally, the CGPS and InSAR measurements were referred to a common date of the SAR acquisition.

3) To match the InSAR pixels and the CGPS stations: the InSAR displacement maps were interpolated to 50×50 m grid. A radius was chosen to guarantee a sufficient number of homogeneous pixels (with high coherence and low velocity dispersion) as close as possible to each CGPS site and the average value for all pixels falling within the circular area was computed. These average values were used for the InSAR and CGPS comparisons.

TABLE II
VELOCITY DATA FOR CGPS STATIONS IN THE ITRF2008 REFERENCE FRAME

Station	N (mm/yr)	E (mm/yr)	U (mm/yr)
CH01	-18.64±0.21	36.35±0.11	-19.27±0.19
CH02	-16.09±0.20	29.43±0.07	-8.33±0.20
DZ01	-16.48±0.20	34.83±0.12	-15.89±0.19
GGSL	-13.68±0.19	33.75±0.10	-25.25±0.18
JHAI	-13.21±0.17	30.57±0.10	-52.20±0.18
KC01	-12.52±0.21	31.95±0.11	-13.23±0.23
KC02	-17.68±0.50	38.83±0.41	-25.23±0.59
NIHE	-10.24±0.17	32.71±0.10	-24.46±0.18
PANZ	-14.09±0.17	31.13±0.10	-21.26±0.18
QING	-19.97±0.23	29.41±0.11	-63.47±0.18
SW01	-5.15±0.17	35.35±0.12	-38.53±0.21
TJA1	-14.04±0.19	31.42±0.11	-25.90±0.22
TJA2	-22.65±0.22	34.19±0.08	-7.12±0.18
TJBD	-16.26±0.19	32.96±0.07	-2.92±0.13
TJBH	-13.17±0.17	33.88±0.10	-18.12±0.18
TJWQ	-14.57±0.18	38.10±0.11	-40.99±0.23
WQCG	-20.80±0.21	35.62±0.07	-22.61±0.13
XQYY	-18.47±0.22	33.13±0.10	-19.23±0.18
YC01	-15.64±0.22	34.48±0.14	-34.91±0.29

III. RESULTS

A. CGPS Results

The 3-D velocities in the ITRF2008 reference frame are shown in Table II and displayed in Fig. 1. The longitude and latitude information of the CGPS stations can be found in Supplementary Material (see Table S1). An examination of the CGPS solutions in the frame of ITRF2008 in Table II indicates horizontal movements at all stations varying from about 5 to 20 mm/yr in the south direction and 29 to 36 mm/yr in the east direction. This motion primarily reflects a rigid motion of the Eurasian plate with respect to ITRF2008. All CGPS stations show negative rates in the vertical direction, indicating land subsidence across the region. A maximum rate of 63.47 mm/yr was found at QING station located around Wangqingtuo Town. The annual and semiannual terms are shown in Table III. The plots of 3-D coordinate changes in the ITRF2008 reference frame for all the CGPS stations are provided in Supplementary Material (see Fig. S1). Inspection of our CGPS results indicates that annual and seasonal signals in the vertical component are small at most stations. The amplitudes of the annual term varying from 3 to 12 mm (average 5.26 mm) are more dominant than the semiannual one ranging from 1 to 3 mm (average 2 mm),

TABLE III
ANNUAL AND SEMIANNUAL TERMS FOR CGPS VERTICAL COMPONENT IN THE ITRF2008 REFERENCE FRAME

	Annual		Semi-annual	
Station	Amplitude (mm)	Phase (month)	Amplitude (mm)	Phase (month)
CH01	5.06	6.05	2.76	9.87
CH02	0.80	1.70	0.78	9.28
DZ01	3.99	4.13	2.57	10.07
GGSL	5.42	3.16	1.81	10.86
JHAI	4.53	3.25	1.05	8.45
KC01	3.66	6.24	2.43	10.65
KC02	6.32	3.29	1.74	8.89
NIHE	7.19	2.78	1.26	9.55
PANZ	5.17	3.74	3.13	10.38
QING	4.86	2.85	1.31	10.18
SW01	4.91	3.32	0.76	3.48
TJA1	3.60	3.12	2.70	9.63
TJA2	4.36	3.46	2.83	9.00
TJBD	4.20	3.98	2.33	10.73
TJBH	5.59	2.26	3.07	10.77
TJWQ	12.49	6.83	2.86	9.87
WQCG	4.86	4.18	2.51	10.80
XQYY	2.59	5.29	2.09	10.75
YC01	4.88	4.28	1.47	9.69

but both are very small compared to the total annual subsidence. The seasonal deformation was mainly due to the earth's surface elastic and porous response to hydrological mass variations [46]. A maximum peak-to-peak amplitude of ∼12.5 mm occurred around July at TJWQ station located on a soft sediment, which displays an upward trend from January to June (see Fig. S1) when the groundwater is continuously extracted for irrigation and a downward trend from July to December when the groundwater is recharged and accumulated from precipitation.

A small subsiding rate at TJA2 and TJBD suggests a relatively stable ground in the northern region far from the coast and can be serve as reference point for datum unification between InSAR and CGPS. The average 3-D coordinate changes of the two CGPS stations were subtracted from the other 17 CGPS stations for each component, as described in Section II. This implementation referred the CGPS measurements in global reference frame to the local reference frame. The local 3-D velocities of the CGPS stations (except TJA2 and TJBD) are shown in Table IV. We noticed that most stations are also subjected to residual movement of 0–9 and 0–5 mm/yr in the north–south and east–west direction, respectively. This could be caused by possible local instability in the horizontal component. A significant north–south motion of 14.3 and 9.22 mm/yr at SW01 and NIHE stations, respectively, were most likely caused by the antenna problem during 2018 (see coordinate time series in Fig. S1), which caused the residual in the horizontal movement.

B. InSAR LOS Deformation Maps

Fig. 4 shows LOS average deformation rates for our study area derived from coherence-based SBAS analysis. The spatial pattern of the deformation maps in Fig. 4, from ascending and

TABLE IV
VELOCITY DATA FOR CGPS STATIONS IN THE LOCAL REFERENCE FRAME

Station	N (mm/yr)	E (mm/yr)	U (mm/yr)
CH01	0.81±0.19	2.77±0.09	-14.25±0.13
CH02	3.37±0.18	-4.15±0.07	-3.31±0.20
DZ01	2.97±0.18	1.26±0.09	-10.87±0.14
GGSL	5.78±0.16	0.18±0.07	-20.23±0.13
JHAI	6.25±0.15	-3.01±0.07	-47.18±0.13
KC01	6.93±0.18	-1.62±0.07	-8.20±0.16
KC02	1.78±0.36	5.24±0.26	-20.20±0.38
NIHE	9.22±0.15	-0.87±0.07	-19.44±0.13
PANZ	5.37±0.15	-2.45±0.07	-16.23±0.14
QING	-0.51±0.21	-4.17±0.08	-58.45±0.12
SW01	14.31±0.14	1.78±0.10	-33.50±0.15
TJA1	5.42±0.17	-2.16±0.08	-20.87±0.17
TJBH	6.29±0.14	0.31±0.07	-13.10±0.13
TJWQ	4.89±0.15	4.52±0.08	-35.96±0.18
WQCG	-1.34±0.19	2.04±0.07	-17.59±0.13
XQYY	0.99±0.20	-0.45±0.08	-14.21±0.13
YC01	3.81±0.17	0.91±0.10	-29.90±0.22

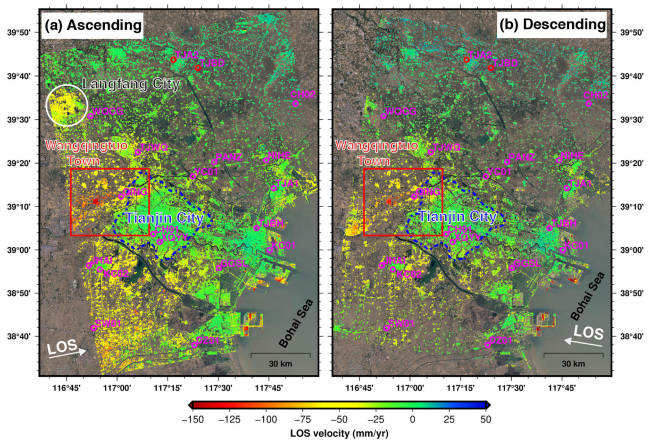

Fig. 4. Sentinel-1 ascending (a) and descending (b) LOS deformation velocities referenced to the local reference frame defined by the two CGPS stations (TJA2 and TJBD, indicated as the red circles in the north). Negative and positive values are corresponding to movement away and toward the radar sensor, respectively. The magenta circles mark the locations of CGPS stations.

descending datasets, are similar. The ground in the downtown of Tianjin city (encircled by the blue dashed line in Fig. 4) was generally stable or slightly subsiding, with average subsidence rate less than 8 mm/yr in the LOS direction. The most conspicuous feature is the large subsidence bowl centered on Wangqingtuo Town (marked as the red box in Fig. 4) in the northwest of Tianjin city, where the observed LOS rate is up to 170 mm/yr. Another subsidence bowl centered on Langfang city [marked with the white circle in Fig. 4(a)] was identified with subsiding rates ranging from 30 to 60 mm/yr, but only covered in the ascending swath. Localized subsidence areas with maximum LOS rates up to 180 mm/yr were clearly identified along the coast on the port, which are related to artificial lands recently reclaimed or built. A comparison of the displacement rates between ascending and descending tracks is illustrated in Fig. 5. The two datasets were consistent, but differences can be

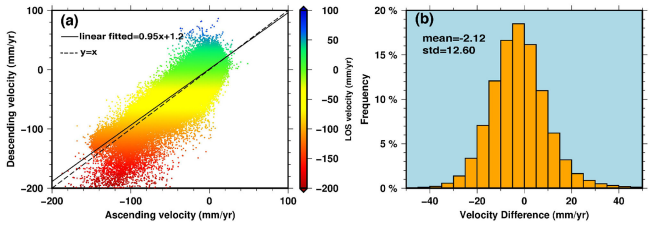

Fig. 5. Correlation and difference analysis between ascending and descending displacement rates.

from noises in both ascending and descending datasets and from the effect of possible horizontal ground motion.

IV. Discussion

A. Comparison Between InSAR and CGPS Measurements

The comparison between CGPS and InSAR displacements from ascending data is shown in Fig. 6 and the same comparison for descending dataset is provided in Supplementary Material (see Fig. S2). For both ascending and descending datasets, the InSAR time-series displacements show good agreement with CGPS, as well as a scatter reduction after correction for the atmospheric delays. After atmospheric correction, the average root-mean-square-error (rmse) between time-series displacements from the two techniques reduced from 15 to 7 mm for the ascending dataset and a similar reduction (from 14 to 7 mm) for the descending dataset. We clearly observed considerable error reductions on those acquisitions (marked by the green ellipses in Fig. 6) during the monsoons (June, July, and August). This is because the water vapor content reaches its maximum and varies very fast during the monsoons, causing a larger propagation delays than in the dry seasons.

The LOS rates of InSAR and CGPS before and after atmospheric corrections are listed in Table V. For the ascending data, the rmse of the LOS velocity between InSAR and CGPS was ∼7 mm/yr before correction and reduced to ∼4 mm/yr after correction. For descending data, the atmospheric correction reduced the RMSE from ∼8 to ∼4 mm/yr. It indicated that the combined InSAR/CGPS results provide both a highly accurate and precise displacement with high spatial resolution. This is a critical information for understanding the link between land subsidence and RLSR.

B. Vertical Land Motion

With datasets from different viewing directions in ascending and descending orbits, the components of horizontal and vertical deformation can be decomposed [47], [48]. Given the near polar orbits of SAR satellites, LOS measurements are more sensitive to displacements in vertical and east–west directions than to the north-south direction. By neglecting the impact of the north–south displacements to the LOS direction, deformation in east–west and up–down directions were resolved by the following matrix of equations:

$$\begin{bmatrix} d_{LOS}^{asc} \\ d_{LOS}^{des} \end{bmatrix} = \begin{bmatrix} -\sin\theta^{asc}\cos\alpha^{asc} & \cos\theta^{asc} \\ -\sin\theta^{des}\cos\alpha^{des} & \cos\theta^{des} \end{bmatrix} \begin{bmatrix} d_{East} \\ d_{Up} \end{bmatrix} \quad (7)$$

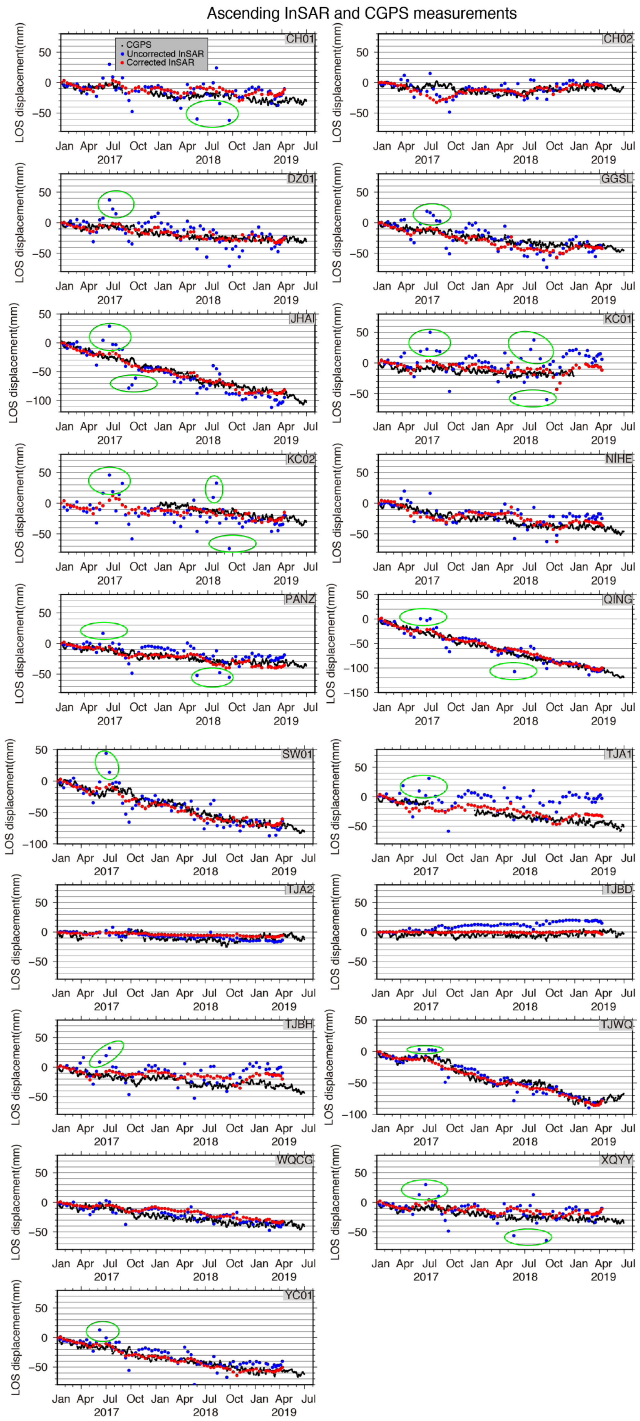

Fig. 6. Comparison of CGPS with InSAR displacements from ascending track. The 3-D CGPS measurements have been projected onto the InSAR LOS vector. Green ellipses display the data points with significant error reduction after atmospheric correction, which are mainly within the monsoons (June, July, and August).

where the subscript asc and des indicate ascending and descending geometries, respectively. In (7), we describe ground deformation (d_{LOS}^{asc} and d_{LOS}^{des}) as discrete displacements, but same description holds for deformation rates. The solution to this equation can be found by the least square algorithm. By applying this decomposition, we obtained the up–down and east–west

TABLE V
COMPARISON BETWEEN INSAR AND CGPS RATES IN LOS DIRECTION

CGPS station	$V^{LOS}_{CGPS,asc}$ (mm/yr)	$V^{a}_{InSAR,asc}$ (mm/yr)	$V^{b}_{InSAR,asc}$ (mm/yr)	$V^{LOS}_{CGPS,des}$ (mm/yr)	$V^{a}_{InSAR,des}$ (mm/yr)	$V^{b}_{InSAR,des}$ (mm/yr)
CH01	-12.36	-7.25	-7.04	-5.53	-7.96	-5.26
CH02	-2.89	1.90	2.73	-5.95	-7.31	-6.62
DZ01	-12.66	-17.70	-12.41	-7.86	-3.83	-6.38
GGSL	-17.30	-22.74	-18.83	-14.33	-20.75	-19.95
JHAI	-37.68	-46.72	-38.85	-38.11	-31.19	-30.00
KC01	-7.21	1.79	-4.74	-6.08	-7.34	-7.36
KC02	-20.73	-15.44	-13.57	-13.28	7.94	-12.78
NIHE	-17.64	-10.46	-13.54	-16.40	-17.36	-16.61
PANZ	-14.11	-11.57	-16.59	-14.21	-11.13	-12.70
QING	-42.60	-45.88	-43.96	-44.08	-39.93	-42.11
SW01	-32.11	-36.06	-32.40	-24.64	-23.15	-21.97
TJA1	-20.75	-1.22	-12.34	-18.10	-18.02	-20.05
TJA2	-11.93	-3.59	-5.39	-8.60	-6.58	-8.98
TJBD	-35.15	-37.91	-37.14	-30.43	-23.35	-27.85
TJBH	-16.17	-14.78	-13.92	-12.62	6.23	-3.77
TJWQ	-11.71	-8.51	-7.47	-9.71	-9.40	-6.79
WQCG	-25.02	-22.29	-25.67	-19.72	-22.15	-23.61
XQYY	-12.36	-7.25	-7.04	-5.53	-7.96	-5.26
YC01	-2.89	1.90	2.73	-5.95	-7.31	-6.62

$V^{LOS}_{CGPS,Asc}$ means the rate of CGPS projected onto ascending LOS direction. $V^{LOS}_{CGPS,Des}$ means the rate of CGPS projected onto descending LOS direction. V^{a}_{InSAR} means the rate of InSAR before atmospheric correction. V^{b}_{InSAR} means the rate of InSAR after atmospheric correction.

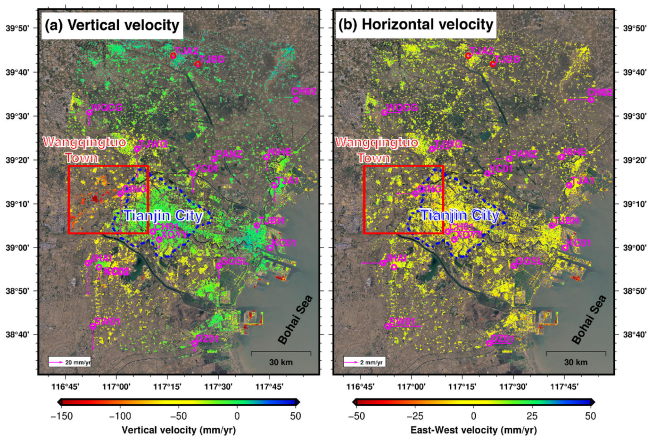

Fig. 7. Vertical and horizontal displacement velocities obtained by decomposition of the LOS velocity from ascending and descending tracks. (a) Vertical (up–down) displacement rates. (b) Horizontal (east–west) displacement rates. CGPS displacements are also indicated with arrows for comparison.

components of the displacement velocities in our study area, as shown in Fig. 7.

From Fig. 7 we can see that ground deformation mainly occurred in the vertical direction while the horizontal component is relatively small. However, the decomposition results are not particularly good due to the previously mentioned methodological aspects (interpolation and assuming a linear displacement rate). Another reason is the fact that the magnitude of the east–west movement is at the levels of subcentimeter per year in many of the coherent pixels, i.e., the same order of the SBAS-InSAR uncertainty. Such decomposition is achievable only when the displacement signal is spatially smooth and well sampled.

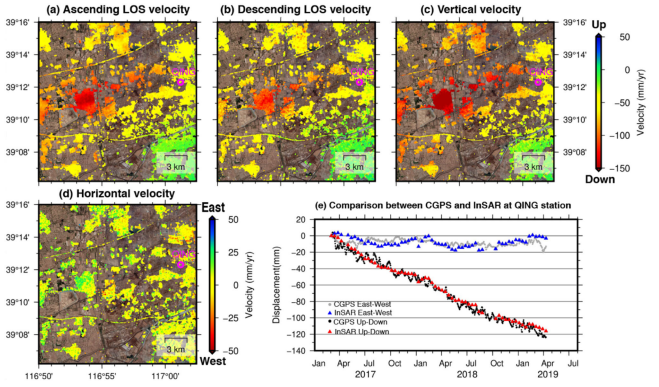

Fig. 8. East–west and vertical deformation in Wangqingtuo Town derived by data combination. (a) Ascending LOS velocity. (b) Descending LOS velocity. (c) Up–down component of deformation. (d) East-west component of deformation. (e) Comparison between InSAR and CGPS at QING station.

In Supplementary Material (see Table S2), we compared the vertical and horizontal displacement rates between InSAR and CGPS. The rmse between CGPS and InSAR is ∼3 mm/yr in the vertical velocity component (good agreement) and ∼5 mm/yr in the east–west velocity component (worse agreement). This again indicates that we have effectively placed the InSAR velocities in the same reference frame as the CGPS data.

We now investigate the large subsidence bowl centered on Wangqingtuo Town in the west of Tianjin city. Groundwater pumping is the main driver of subsidence in this area, which has been discussed and documented in many literatures [6], [31], [32]. The horizontal displacement induced by aquifer compaction can be strong and its damages to infrastructures have been reported [32]. Fig. 8 displays a close-up view of LOS velocities in Wangqingtuo town along with the up–down and east–west components derived by data decomposition. The CGPS station (QING) located in this area was used for comparison as shown in Fig. 8(e) and a good agreement between the two datasets for both vertical and east-west components was found.

C. Land Subsidence Along the Coastal Region

In Tianjin, the demand of land resources has steadily risen following the ongoing economic growth after the Tianjin Binhai New Area (TBNA) becoming part of the National Development Strategy in 2005. The coastal area prior to development was dominated by mudflats, salt marshes (and salterns), and coastal shallows. The littoral zone is wide and slopes gently: the 0 m isobath (the intertidal flats) extends to 3–8 km from shore at a slope of 0.71–1.28%, the −5 m isobath extends 14–18 km from shore, and the −10 m isobath reaches 22–36 km from shore. These characteristics suggest that land reclamation to the sea is a cost-effective option to meet the urgent demand of land resources. Harbors in Tianjin are thus by necessity largely man-made through dredging and reclamation. The expansion of artificial land caused coastlines extending further out to the sea, as interpreted in Fig. 9(b) and Supplementary Material (see Fig. S3). The length of coastline in this area increased by 184.82 km and the reclamation area increased by 357.35 km^2 during the period 1995–2015 [49]. The reclamation lands have been

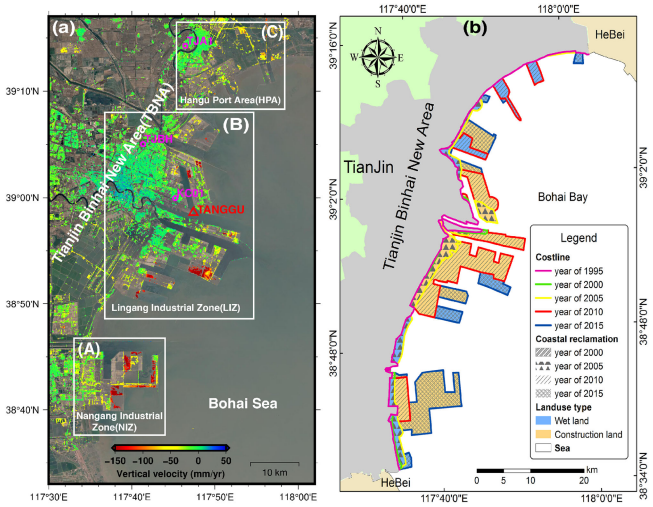

Fig. 9. (a) Vertical land motion rates focused on Tianjin coastal region. (b) Coastline changes from 1995 to 2015 (modified from [49]). The three white boxes: (A) corresponding to Nangang Industrial Zone (NIZ), (B) corresponding to Lingang Industrial Zone (LIZ), and (C) corresponding to Hangu Port Area (HPA).

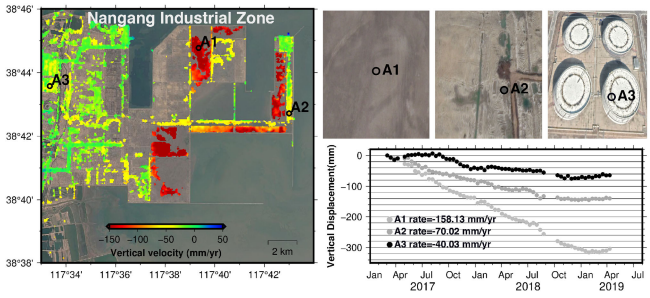

Fig. 10. Land subsidence velocity focused on Nangang Industrial Zone and displacement time series at three selected points (marked by black circles A1, A2, and A3). Blowup images for the locations of these three points are shown.

utilized to build infrastructures including airports, oil facilities, ports, and highways, etc. Subsidence process associated with land reclamation were observed in Fig. 9(a) which can pose risk to infrastructures built on the land. In the following, we divided the discussion into three subsections for the three coastal areas [indicated as white boxes in Fig. 9(a)].

1) Subsidence in Nangang Industrial Zone: One of the first mega construction project in Tianjin is the harbor expansion of Nangang port through land reclamation. The reclaimed areas were used for the establishment of the Nangang Industrial Zone (NIZ), which is positioned to be a world-class petrochemical industry base. The total planned area of the industrial zone is 200 km^2, and about 75% of the land is obtained by reclamation [50]. Remarkable ground settlement can be seen in Fig. 10. The displacement time series at selected three points (A1, A2, and A3) are also shown.

The low stability of the soil layer in the newly reclaimed area plus the building loads are suggested as the main driver of land subsidence in NIZ. The time series analysis at A3 point exhibits a moderate subsidence rate of 40.03 mm/yr. This point is located on a petrochemical plant. The ground subsidence is a matter of concern to the safety of the petrochemical facilities built on this area. Points A1 and A2 displayed a more significant subsidence, especially the point A1 where it is located on the area filling by the disposal of dredged material. Fresh hydraulic fill mud in the process of land reclamation will take the procedure of grain sediment, self-weight compression and drainage consolidation, causing the high rate of land subsidence. The point A2 is located on a newly constructed seawall surrounding the reclamation areas, such subsidence map is important to evaluate the stability of the cofferdam for preventing the flow of water into the reclaimed areas.

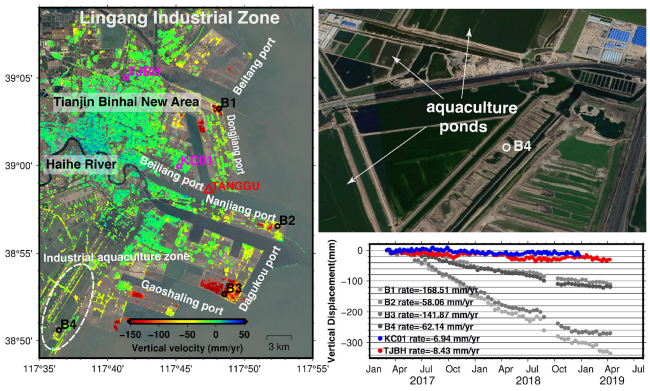

Fig. 11. Land subsidence velocity focused on Lingang Industrial Zone and displacement time series at four selected points (marked by black circles B1, B2, B3, and B4). The magenta circles show the two CGPS stations (KC01 and TJBH) located within this region. The white ellipse indicates clustered aquaculture farms. The area where B4 resides is surrounded by aquaculture ponds, showing rapid subsidence at rate of 62.14 mm/yr.

2) Subsidence in Lingang Industrial Zone: Lingang Industrial Zone (LIN), located in the south intertidal area of Haihe River estuary, is a large-scale sea reclamation project with a total planned area of 99.58 km^2. The detected subsiding rates are as high as 170 mm/yr, as shown in Fig. 11. These localized areas with rapid rates (appear in red) are mainly located on the newly reclaimed port areas near to the coastlines. Monitoring data measured by extensometers in LIN indicated that the compaction within the layer with a depth of 100-400m was small and the groundwater table in deep aquifer were stable [51]. This suggests that the deep groundwater exploitation is not the main driver for the rapid subsidence on the ports. Instead, the natural sedimentation process of dredged mud causes this high subsidence rates.

Displacement time series at four selected points (B1, B2, B3, and B4) along the coastline are also shown in Fig. 11. Attention should pay to B2 on Nanjiang port that it is located in areas built with infrastructures (roads, harbor facilities and underground pipelines, etc.) which can be severely damaged from differential settling in such areas with high subsidence gradients. The inland areas away from the coast exhibit stable or slightly subsidence, which is confirmed by the two CGPS stations (KC01 and TJBH) with subsiding rates less than 10 mm/yr (the comparison between InSAR and CGPS at these two sites refer to Fig. 6). For the inland region, aquifer-system compaction due to groundwater

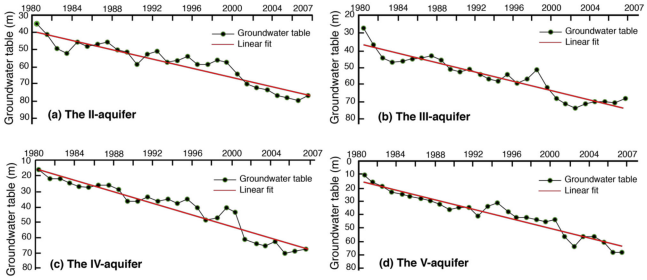

Fig. 12. Groundwater table changes in Hangu district during the period 1980–2007. Modified from [30].

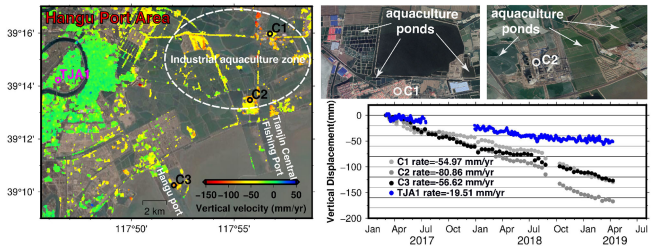

Fig. 13. Land subsidence velocity focused on Hangu Port Area and displacement time series at three selected points (marked by circles C1, C2, and C3). The magenta circle shows the CGPS station (TJA1) located within this region. The white ellipse indicates clustered aquaculture farms. The areas where C1 and C2 reside are surrounded by aquaculture ponds, showing rapid subsidence with rates of 54.97 and 80.86 mm/yr, respectively.

extraction is responsible for the majority of land subsidence [52].

Like many coastal areas, the coastline of the Tianjin is dominated by aquaculture industry. At present, there are 122 aquaculture households in TBNA, and annually more than 20 million m^3 of groundwater were used [12]. Most aquaculture activities are generally located along the coastline, with fish farms and shrimp ponds clustered. Over-exploitation of saline groundwater in aquaculture had caused severe land subsidence. The subsidence on those areas surrounded by aquaculture farms is rapid (>50 mm/yr), localized and patchy, as shown in Fig. 11(indicated by white ellipse). The temporal evolution of subsidence at point B4 located in this aquaculture zone is shown in Fig. 11, which is subsiding at a rapid rate of 62.14 mm/yr. Fortunately, countermeasures have been adopted to deal with this problem. In 2018, the local government of TBNA announced a ban on aquaculture farmers in the jurisdiction using saline groundwater. Illegal and undocumented aquaculture wells have been sealed. In addition, Tianjin has received more than 1.8 billion cubic meters of water via the NSWTP since December 2014, which also provides support in reducing groundwater consumption [12]. Both the rates of groundwater extraction and land subsidence have slowed down, and note that even a slight land uplift occurred in the downtown of TBNA.

3) Subsidence in Hangu Port Area: Hangu Port Area (HPA) is located in the northeast of Tianjin city. The groundwater in Hangu district has been over-exploited for a long time, which led to a dramatic drop in the water table, as shown in Fig. 12 (adapted from [30]). The dropping rate of water levels is around 2 m/yr from 1980 through 2007. The average measured land subsidence rates in Hangu district were about 58.2 mm/yr in the 1980s, 44.8 mm/yr in the 1990s, and 33 mm/yr after 2000 [30]. The InSAR-measured average subsidence rate in downtown area of Hangu district during the study period is about 20 mm/yr. A similar subsidence rate of 19.5 mm/yr was observed by the CGPS station (TJA1) located in the downtown area. This also reflects the alleviation of land subsidence in the central city area of HPA. However, more significant subsidence was found at points C1 (54.97 mm/yr) and C2 (80.86 mm/yr) located in the rural areas, and at point C3 (56.62 mm/yr) located on the port.

In the suburbs and rural areas, people are still extensively relying on groundwater pumping for the purposes of households, agricultural irrigation and especially aquaculture industry. The aquaculture facilities are mainly located in the northern HPA (white ellipse in Fig. 13). As discussed in the above subsection, groundwater pumping at these aquaculture-dominated zones has caused significant land subsidence, as shown at the points of C1 and C2. The Hangu port is under construction, the natural settling of fill and disturbed soils on this newly reclaimed land is responsible for the remarkable subsidence at point C3. But settling of fill and disturbed soils only contributes to the local subsidence in the port areas, it is not likely to be contributing to regional land subsidence.

TABLE VI
SEA LEVEL RISE AND LAND SUBSIDENCE IN TIANJIN

Period	SLR (mm/yr)	Land subsidence (mm/yr)	RSLR (mm/yr)	Agency/ Publication
Global Data				
1901-2010	1.70	-	-	IPCC
1993-2018	3.15	-	-	IPCC
China coastal region				
1980-2018	3.3	-	-	CSLB
2009-2018	5.5	-	-	CSLB
Tianjin coastal region				
1950-1986	1.4	-	-	[54]
1986-2008	4.7	-	-	[54]
1985-1996	1.5	13	14.5	[55]
1996-2003	1.5	28	29.5	[55]
2018-2050	4.76	20	24.76	[23]

IPCC: The Intergovernmental Panel on Climate Change.
CSLB: China Sea Level Bulletin [53].

D. Relative Sea Level Trends Along the Coastal Region

Determining the spatial distribution of RSLR is important because it has the most direct impact on coastal planning and society, such as the seawall design must account for the RSLR in different places. As observed in Figs. 10, 11, and 13, significant spatial variability in rates of land motion exists around the region, which contributes to spatially varying rates of relative SLR. Multiple types of data have described land subsidence and SLR in the Tianjin coastal area (see Table VI). We can see that the magnitude of land subsidence in Tianjin coastal region is much greater than global/regional SLR, which is largely

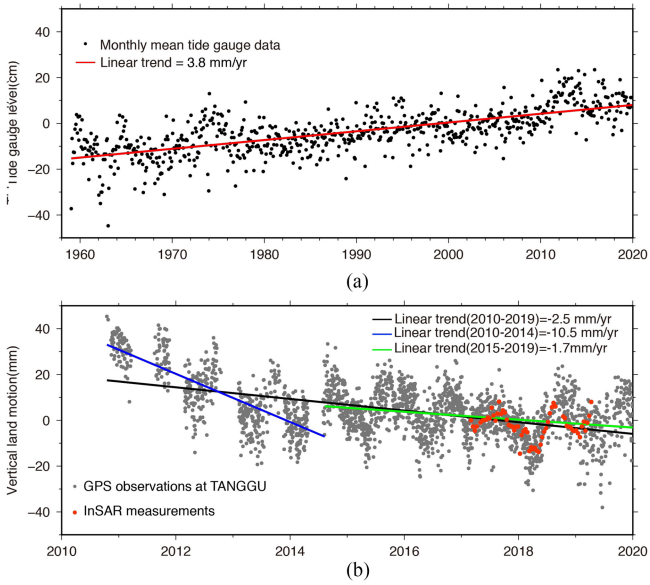

Fig. 14. (a) Sea level change and long-term linear trend (3.8 mm/yr) from TANGGU tide gauge station. (b) Vertical land displacement from the GPS station (grey points) collocated with TANGGU station and comparison with measurements from InSAR (red points). The land subsidence rates have slowed down as shown by linear trends in different periods.

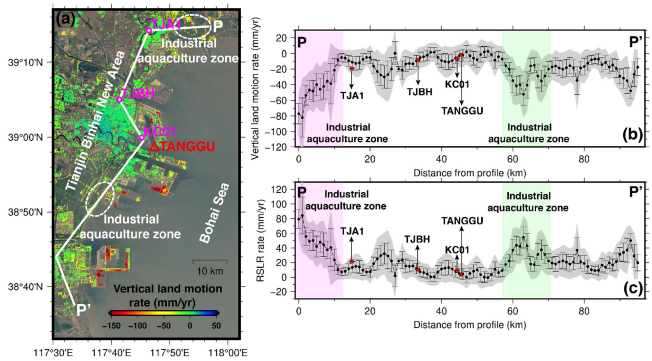

Fig. 15. (a) Vertical land motion rates from InSAR along the Tianjin coastal region. The two white ellipses indicate clustered aquaculture farms. (b) Cross-section (P-P') of vertical land motion rates along the coast. The red squares indicate the locations of CGPS stations (TJA1, TJBH, KC01, and TANGGU). (b) Cross-section of relative sea level change referenced to the TANGGU tide gauge. Profile was formed by taking the mean velocity value in a 500 m circular area, spaced every 1000 m along the profile. The black line indicates the standard deviation (σ) of displacements of selected InSAR pixels inside the circular area. Gray shading indicates 2σ uncertainty of the velocity from each circular area along the profile.

responsible for the RSLR in the low-relief area. But these results or projections only relying on sparse tide gauge stations, which cannot reflect the spatial extent of relative sea level trends. In this study, we combined TANGGU tide gauge records and InSAR land motion measurements to examine the impact of spatially variable land subsidence on relative sea level trends along the coast of Tianjin.

TANGGU tide gauge station (see location in Fig. 1) was constructed in March 1949 and continuous data is available from the 1950s. Monthly mean tide gauge data at TANGGU station shows a rising trend of RSLR 3.8 mm/yr from 1959 to 2019 [see Fig. 14(a)], which is larger than the rising rate of global sea level from the Intergovernmental Panel on Climate Change (IPCC). The land area where this tide gauge resides suffered from significant land subsidence in the past decades. However, tidal gauges do not distinguish between the sea level that is rising and the land that is sinking, i.e., tide gauge only measures RSLR. A collocated CGPS station was built at this tide gauge in 2010 and the data show land subsidence with a rate of 2.5 mm/yr from 2010 to 2019 [see Fig. 14(b)]. The trends of land subsidence apparently slowed down after 2014 because stricter practices have been enforced to control groundwater pumping, that the rate was 10.5 mm/yr before 2014 and reduced to 1.7 mm/yr after 2015. The vertical displacement from InSAR during the period of 2017–2019 is in good agreement with GPS at TANGGU tide gauge [see Fig. 14(b)], further validate the accuracy of the InSAR results.

The collocated CGPS station enables local land motion to be separated from the rising sea at TANGGU tide gauge. By further combining high resolution of land motion from InSAR, the spatial variation of RLSR along Tianjin coastal region can be obtained. To convert the rate of RSLR at TANGGU station (r_{TG} $= 3.8$ mm/yr) to the RSLR rates at other locations ($r(x)$), we first computed the vertical land motion rate at the TANGGU tide gauge station (L_{TG}) from the collocated CGPS station during the recent period 2015–2019 [the green line in Fig. 14(b)]. The InSAR vertical land motion rates at other locations along the coast (L(x)) is then subtracted from the sum of r_{TG} and L_{TG}, which give rates of RSLR along the coast [56], [57]

$$r\ (x) = r_{TG}\ + L_{TG} - L\,(x) \tag{8}$$

We examined one cross-section P-P' (see location in Fig. 15) along the coast and estimated the rates of RSLR by taking the mean value in a 500 m circular area, spaced every 1000 m along the profile. Along this cross-section, extending from the northern Hangu district to the southeast of Tianjin, the vertical land motion rates are variable ranging from a maximum land subsidence rate of 82 mm/yr located in the aquaculture area in the north [see the white ellipse in northern region in Fig. 15(a)], to a land uplift of 2.6 mm/yr in the urban area of TBNA. The spatial variability of relative sea level changes ranges from a low of -1 mm/yr to a high of 84.2 mm/yr along the profile, which was obviously due to the local processes of vertical land motion. These results suggest that in this coastal region, simply using the TANGGU tide gauge station alone would provide a poor indication of relative sea level trends – for the profile with a length of 96 km along the coast, the sign of RSLR would be reversed. Our results emphasize the need for the high spatial resolution measurements of land displacement provided by InSAR in evaluation of the regional RSLR.

We have shown that groundwater pumping at the aquaculture-dominated zones along the coastline induce two peaks of land subsidence rates along the profile [see Fig. 15(b)], with maximum rates of 82 and 52 mm/yr in the north and south, respectively. These subsidence rates greatly increase the magnitude of RSLR at the two aquaculture zones to 84.2 and 54.3 mm/yr for

the north and south zone [see Fig. 15(c)], respectively. These rates exceed local and global average SLR by nearly 30 times.

E. Implications and Limitations

The land subsidence reported in this study has serious implications for the sustainable development of aquaculture-dominated coastlines. Because aquaculture is a vital protein source for hundreds of million people, the fastest growing food producing sector worldwide and potential to support future food security in a global context. Human consumed more farmed species than capture fisheries for the first time in 2014 and global aquaculture production increased more than double from 32.4 million tons in 2000 to 82.1 million tons in 2018 [58]. Asia generates 90% of the world's aquaculture volume which is primarily produced by pond systems in fertile coastal environments. The coastal ecosystems are inherently fragile and vulnerable to climatic changes, such as flooding, temperature, precipitation, and SLR, while the situation is worsening due to groundwater-induced subsidence at coastal aquaculture zones. We have shown that the subsidence rates at aquaculture farms significantly exceed the order of global average SLR, which suggests that the greatest threat to the sustainable development of coastal aquaculture may not be global SLR but RSLR due to land subsidence from groundwater pumping.

However, it is fair to point out that advancements of the InSAR technique are still needed to meet the requirements of submillimeter per year accuracy for studies on long term trends in relative sea levels. The most important research areas include coherent points detection, atmospheric delay correction, and height system unification by using SAR transponders. Even though the high repeating rate (12 days) and temporally uniform distribution of Sentinel-1 data and the advanced SBAS method were used in our study, which did not prevent from coherence loss over vegetated areas, subsequently reducing the density of coherent pixels and the reliability of the phase unwrapping over a large spatial extent. This limitation underlines the need of the advancement to increase the spatial density of persistent pixels, such as by SqueeSAR^{TM} method [59], especially over vegetated areas along the coastlines. In addition, the high repeating rate of Sentinel-1 data does not necessary implies smaller atmospheric noises, as the atmosphere varies from day to day, and in space. In this study, we assumed the atmospheric delays are randomly distributed in time and used a common-point stacking to mitigate the delays. However, the estimates of displacement may be biased as the atmospheric delay can be temporally correlated and therefore causes the assumption of random noises of delays incorrect [60], [61]. Another drawback is that the displacements obtained by InSAR are relative measurements with respect to a reference point, and if the chosen reference point is unstable in reality, this can lead to biased measurements, which makes it impossible to evaluate the long-term SLR. In this article, we connected the InSAR-derived velocities to a local reference system (a "datum") by minimizing the differences between displacement estimates obtained from two CGPS stations and the nearby InSAR pixels. The displacement of the "nearby InSAR pixels" is then stochastic, and the errors can be propagated. This can be resolved by collocated installation of corner reflector or active radar transponder [62] at the tide gauge.

V. Conclusion

This article investigated recent (2017–2019) land subsidence in Tianjin coastal region through analysis of space-borne InSAR and CGPS measurements, and spatially evaluated the relative sea level trends along the coastline with an unprecedented high-spatial resolution and precision. Our findings show that recent land subsidence rates in Tianjin downtown appears to slow down with respect to the last 50 years. This might benefit from the SNWTP which has provided more than 1.8 billion cubic meters of water for Tianjin city since 2014 and reduced groundwater consumption. Nonetheless, significant land subsidence was found along the coastline, localized in the reclaimed harbors and in industrial aquaculture zones. The rapid subsidence rates in the areas of land reclamation was due to the natural consolidation process of the dredged muds and the compaction rates will reduce over time. However, more emphasis of groundwater management strategies needs to be put on the aquaculture-dominated areas where they are heavily relying on saline groundwater. The rates of land subsidence are as high as 82 mm/yr in aquaculture zones due to groundwater pumping, which cause local sea level to rise nearly 30 times faster than the global average. New insights of land subsidence and local SLR could help the country's regulators to make decision on ensuring the sustainable development of the aquaculture industry along the coastline.

Much consideration has been given to the impacts of global SLR on coastal region, but less caution is given to RSLR produced by land subsidence. The land motion mapped by InSAR and CGPS in Tianjin coastal region have shown that the land subsidence is much larger than the magnitude of global/regional average SLR. Furthermore, the high degree of spatial variability in rates of land subsidence result in the rates of RSLR varies considerably from place to place. This suggests a single tide gauge evaluation of regional RSL would have limited applicability and emphasizes the need of the high-spatial resolution measurements provided by InSAR. The freely available data with large illuminated tracks (250 km wide) and high repeat rate (6 or 12 days) provided by the Sentinel-1 constellation, make it an attractive source of data to study land motion in coastal regions with a large spatial extent.

Acknowledgment

The Single Look Complex (SLC) images from Sentinel-1 satellite, freely distributed by European Space Agency (ESA) and obtained from Alaska Satellite Facility (ASF) data search vertex (https://www.asf.alaska.edu). Some of the figures were generated using Generic Mapping Tools.

References

[1] M. Han, L. Wu, J. Hou, G. Liu, G. Zhao, and Z. Zhang, "Sea-level rise and the North China coastal plain: A preliminary analysis," *J. Coastal Res.*, no. 14, pp. 132–150, 1995.

[2] F. Cai, X. Su, J. Liu, B. Li, and G. Lei, "Coastal erosion in China under the condition of global climate change and measures for its prevention," *Prog. Natural Sci.*, vol. 19, no. 4, pp. 415–426, 2009.

[3] J. Ma, Z. Zhou, Q. Guo, S. Zhu, Y. Dai, and Q. Shen, "Spatial characterization of seawater intrusion in a coastal aquifer of Northeast Liaodong bay, China," *Sustainability*, vol. 11, no. 24, 2019, Art. no. 7013.

[4] D. Han and M. Currell, "Delineating multiple salinization processes in a coastal plain aquifer, northern China: Hydrochemical and isotopic evidence," *Hydrol. Earth Syst. Sci.*, vol. 22, pp. 3473–3491, 2018.

[5] L. Zhu, C. Jiang, Y. Wang, Y. Peng, and P. Zhang, "A risk assessment of water salinization during the initial impounding period of a proposed reservoir in Tianjin, China," *Environ. Sci. Process Impacts*, vol. 15, no. 9, pp. 1743–1751, 2013.

[6] L. Yi, F. Zhang, H. Xu, S. Chen, W. Wang, and Q. Yu, "Land subsidence in Tianjin, China," *Environ. Earth Sci.*, vol. 62, pp. 1151–1161, 2010.

[7] Q. Zhao, B. Zhang, Y. Yao, W. Wu, G. Meng, and Q. Chen, "Geodetic and hydrological measurements reveal the recent acceleration of groundwater depletion in North China Plain," *J. Hydrol.*, vol. 575, pp. 1065–1072, 2019.

[8] J. P. Moiwo, F. Tao, and W. Lu, "Analysis of satellite-based and in situ hydro-climatic data depicts water storage depletion in North China Region," *Hydrol. Process.*, vol. 27, no. 7, pp. 1011–1020, 2013.

[9] W. Feng, M. Zhong, J. M. Lemoine, R. Biancale, H. T. Hsu, and J. Xia, "Evaluation of groundwater depletion in North China using the gravity recovery and climate experiment (GRACE) data and ground-based measurements," *Water Resour. Res.*, vol. 49, no. 4, pp. 2110–2118, 2013.

[10] Z. Huang *et al.*, "Subregional-scale groundwater depletion detected by GRACE for both shallow and deep aquifers in North China Plain," *Geophys. Res. Lett.*, vol. 42, no. 6, pp. 1791–1799, 2015.

[11] H. Gong *et al.*, "Long-term groundwater storage changes and land subsidence development in the North China Plain (1971–2015)," *Hydrogeol. J.*, vol. 26, no. 5, pp. 1417–1427, 2018.

[12] Xinhua, "Tianjin to tighten groundwater use," *Xinhua News*, 2017. [Online]. Available: https://www.chinadaily.com.cn/china/2017-12/01/content_35159066.htm

[13] T. G. Farr *et al.*, "The shuttle radar topography mission," *Rev. Geophys.*, vol. 45, no. 2, pp. 1–33, 2007.

[14] D. P. S. Bekaert, B. D. Hamlington, B. Buzzanga, and C. E. Jones, "Spaceborne synthetic aperture radar survey of subsidence in Hampton roads, Virginia, USA," *Sci. Rep.*, vol. 7, no. 1, pp. 1–9, 2017.

[15] J. Eggleston and J. Pope, "Land Subsidence and Relative Sea-Level Rise in the Southern Chesapeake Bay Region," *U.S. Geological Surv. Circular*, 2013, doi: 10.3133/cir1392.

[16] H. Z. Abidin, H. Andreas, I. Gumilar, and J. J. Brinkman, "Study on the risk and impacts of land subsidence in Jakarta," *Proc. Int. Assoc. Hydrol. Sci.*, vol. 372, pp. 115–120, 2015.

[17] L. Bayuaji, J. T. S. Sumantyo, and H. Kuze, "ALOS PALSAR D-InSAR for land subsidence mapping in Jakarta, Indonesia," *Can. J. Remote Sens.*, vol. 36, no. 1, pp. 1–8, Jan. 2010.

[18] L. E. Erban, S. M. Gorelick, and H. A. Zebker, "Groundwater extraction, land subsidence, and sea-level rise in the Mekong delta, Vietnam," *Environ. Res. Lett.*, vol. 9, no. 8, 2014, Art. no. 84010.

[19] P. S. J. Minderhoud *et al.*, "Impacts of 25 years of groundwater extraction on subsidence in the Mekong delta, Vietnam," *Environ. Res. Lett.*, vol. 12, no. 6, 2017.

[20] J. Wang, W. Gao, S. Xu, and L. Yu, "Evaluation of the combined risk of sea level rise, land subsidence, and storm surges on the coastal areas of Shanghai, China," *Climatic Change*, vol. 115, no. 3–4, pp. 537–558, 2012.

[21] J. Yang, "Land subsidence reduced to safe level," *Shanghai Daily*, 2016. [Online]. Available: https://archive.shine.cn/metro/public-services/Land-subsidence-reduced-to-safe-level/shdaily.shtml

[22] S. H. Liu *et al.*, "Vertical motions of tide gauge stations near the Bohai Sea and Yellow Sea," *Sci. China Earth Sci.*, vol. 58, no. 12, pp. 2279–2288, 2015.

[23] F. Wang, J. Li, P. Shi, Z. Shang, Y. Li, and H. Wang, "The impact of sea-level rise on the coast of Tianjin-Hebei, China," *China Geol.*, vol. 2, no. 1, pp. 26–39, 2019.

[24] M. Ren, "Relative sea-level changes in China over the last 80 years," *J. Coastal Res.*, vol. 9, no. 1, pp. 229–241, 1993.

[25] S. Mazzotti, A. Lambert, M. Van der Kooij, and A. Mainville, "Impact of anthropogenic subsidence on relative sea-level rise in the Fraser River delta," *Geology*, vol. 37, no. 9, pp. 771–774, 2009.

[26] H. E. Pelling, K. Uehara, and J. A. M. Green, "The impact of rapid coastline changes and sea level rise on the tides in the Bohai Sea, China," *J. Geophys. Res. Ocean.*, vol. 118, no. 7, pp. 3462–3472, 2013.

[27] J. Du *et al.*, "Tidal response to sea-level rise in different types of estuaries: The importance of length, bathymetry, and geometry," *Geophys. Res. Lett.*, vol. 45, no. 1, pp. 227–235, 2018.

[28] M. D. Pickering *et al.*, "The impact of future sea-level rise on the global tides," *Continental Shelf Res.*, vol. 142, no. February, pp. 50–68, 2017.

[29] Y. Li, H. Zhang, C. Tang, T. Zou, and D. Jiang, "Influence of rising sea level on tidal dynamics in the Bohai sea," *J. Coastal Res.*, vol. 74, pp. 22–31, 2016.

[30] H. Hu and A. Gong, "Study on deep groundwater evolution in Hangu district of Tianjin," *Ground Water*, vol. 36, no. 2, pp. 22–24, 2014.

[31] P. Liu *et al.*, "Anatomy of subsidence in Tianjin from time series InSAR," *Remote Sens*, vol. 8, no. 3, 2016, Art. no. 266.

[32] Q. Luo, D. Perissin, H. Lin, Y. Zhang, and W. Wang, "Subsidence monitoring of Tianjin suburbs by TerraSAR-X persistent scatterers interferometry," *IEEE J. Sel. Topics Appl. Earth Obs. Remote Sens.*, vol. 7, no. 5, pp. 1642–1650, May 2014.

[33] Q. Luo, D. Perissin, Y. Zhang, and Y. Jia, "L- and X-band multi-temporal InSAR analysis of Tianjin subsidence," *Remote Sens.*, vol. 6, no. 9, pp. 7933–7951, 2014.

[34] C. Zhu, Y. Zhang, J. Zhang, L. Zhang, S. Long, and H. Wu, "Recent subsidence in Tianjin, China: Observations from multi-looking TerraSAR-X InSAR from 2009 to 2013," *Int. J. Remote Sens.*, vol. 36, no. 23, pp. 5869–5886, 2015.

[35] S. Higgins, I. Overeem, A. Tanaka, and J. P. M. Syvitski, "Land subsidence at aquaculture facilities in the Yellow River delta, China," *Geophys. Res. Lett.*, vol. 40, no. 15, pp. 3898–3902, 2013.

[36] T. A. Herring, R. W. King, and S. C. McClusky, "GAMIT reference manual. Release 10.4," *Mass. Inst. Technol.*, Cambridge, U.K., 2010. [Online]. Available: https://geo.gob.bo/portal/IMG/pdf/intro_gg_1_.pdf

[37] R. Nikolaidis, "Observation of geodetic and seismic deformation with the global positioning system," Ph.D. dissertation, Univ. Calif., San Diego, USA, 2002.

[38] D. Sandwell, R. Mellors, X. Tong, M. Wei, and P. Wessel, "Open radar interferometry software for mapping surface deformation," *Eos, Trans. Amer. Geophys. Union*, vol. 92, no. 28, pp. 2011–2011, 2011.

[39] X. Xu, D. T. Sandwell, E. Tymofyeyeva, A. Gonzalez-Ortega, and X. Tong, "Tectonic and anthropogenic deformation at the Cerro Prieto geothermal step-over revealed by Sentinel-1A InSAR," *IEEE Trans. Geosci. Remote Sens.*, vol. 55, no. 9, pp. 5284–5292, Sep. 2017.

[40] C. W. Chen and H. A. Zebker, "Two-dimensional phase unwrapping with use of statistical models for cost functions in nonlinear optimization," *J. Opt. Soc. Amer. A*, vol. 18, pp. 338–351, 2001.

[41] T. Ole, "GNU parallel: The command-line power tool," *Login USENIX Mag.*, vol. 36, no. 1, pp. 42–47, 2011.

[42] P. Berardino, G. Fornaro, R. Lanari, and E. Sansosti, "A new algorithm for surface deformation monitoring based on small baseline differential SAR interferograms," *IEEE Trans. Geosci. Remote Sens.*, vol. 40, no. 11, pp. 2375–2383, Nov. 2002.

[43] X. Tong and D. Schmidt, "Active movement of the cascade landslide complex in Washington from a coherence-based InSAR time series method," *Remote Sens. Environ.*, vol. 186, pp. 405–415, 2016.

[44] R. Hanssen, *Radar Interferometry: Data Interpretation and Error Analysis*. New York, NY, USA: Kluwer, 2001.

[45] E. Tymofyeyeva and Y. Fialko, "Mitigation of atmospheric phase delays in InSAR data, with application to the eastern California shear zone," *J. Geophys. Res. Solid Earth*, vol. 120, no. 8, pp. 5952–5963, 2015.

[46] R. Liu, R. Zou, J. Li, C. Zhang, B. Zhao, and Y. Zhang, "Vertical displacements driven by groundwater storage changes in the north China plain detected by GPS observations," *Remote Sens.*, vol. 10, no. 2, pp. 1–13, 2018.

[47] T. Fuhrmann and M. C. Garthwaite, "Resolving three-dimensional surface motion with InSAR: Constraints from multi-geometry data fusion," *Remote Sens.*, vol. 11, no. 3, 2019, Art. no. 241.

[48] M. Motagh *et al.*, "Quantifying groundwater exploitation induced subsidence in the Rafsanjan plain, southeastern Iran, using InSAR time-series and in situ measurements," *Eng. Geol.*, vol. 218, pp. 134–151, Feb. 2017.

[49] W. Chen *et al.*, "Monitoring and analysis of coastal reclamation from 1995-2015 in Tianjin Binhai New Area, China," *Sci. Rep.*, vol. 7, no. 1, pp. 1–12, 2017.

[50] L. Gao, "Engineering problems and countermeasures of land reclamation in Tianjin Nangang industrial zone," M.S. thesis, Tianjin Univeristy, Tianjin, China, 2015.

[51] X. Lv and J. Bai, "Effect of land subsidence on planning and construction of Lingang industrial district in Tianjin and the countermeasures," in *Proc. Int. Symp. Urban Geol.*, 2010, pp. 56–59.

[52] Q. Yu, "Analysis of land subsidence of negative landform region in Tianijn Binhai New Area," M.S. thesis, Tianjin Univeristy, Tianjin, China, 2012.
[53] P. Ministry of Natural Resources, "China sea level bulletin 2018," Beijing, China, 2019.
[54] X. Li, X. Sun, S. Wang, F. Ye, and Y. Li, "Characteristic analysis of Tianjin offshore tide," *Mar. Sci. Bull.*, vol. 13, no. 1, pp. 40–49, 2011.
[55] X. Yang and Z. Wang, "Analysis of the latest development and tendency of relative sea-level change in Tianjin, China," *Earth Environ.*, vol. 42, no. 2, pp. 157–161, 2014.
[56] B. A. Brooks *et al.*, "Space geodetic determination of spatial variability in relative sea level change, Los Angeles basin," *Geophys. Res. Lett.*, vol. 34, no. 1, pp. 1–6, 2007.
[57] C. Poitevin, G. Wöppelmann, D. Raucoules, G. L. Cozannet, M. Marcos, and L. Testut, "Vertical land motion and relative sea level changes along the coastline of Brest (France) from combined space-borne geodetic methods," *Remote Sens. Environ.*, vol. 222, pp. 275–285, 2019.
[58] FAO, "The state of world fisheries and aquaculture 2020. Sustainability in action," Rome, Italy, 2020. [Online]. Available: http://www.fao.org/documents/card/en/c/ca9229en.
[59] A. Ferretti, A. Fumagalli, F. Novali, C. Prati, F. Rocca, and A. Rucci, "A new algorithm for processing interferometric data-stacks: SqueeSAR," *IEEE Trans. Geosci. Remote Sens.*, vol. 49, no. 9, pp. 3460–3470, Sep. 2011.
[60] C. Yu, Z. Li, and N. T. Penna, "Triggered afterslip on the southern Hikurangi subduction interface following the 2016 Kaikōura earthquake from InSAR time series with atmospheric corrections," *Remote Sens. Environ.*, vol. 251, 2020, Art. no. 112097.
[61] D. P. S. Bekaert, R. J. Walters, T. J. Wright, A. J. Hooper, and D. J. Parker, "Statistical comparison of InSAR tropospheric correction techniques," *Remote Sens. Environ.*, vol. 170, pp. 40–47, 2015.
[62] P. Mahapatra, H. van der Marel, F. van Leijen, S. Samiei-Esfahany, R. Klees, and R. Hanssen, "InSAR datum connection using GNSS-augmented radar transponders," *J. Geodesy*, vol. 92, no. 1, pp. 21–32, 2018.

Wei Tang received the Ph.D. degree in photogrammetry and remote sensing from the State Key Laboratory of Information Engineering in Surveying, Mapping and Remote Sensing, Wuhan University, Wuhan, China, in 2017.

In 2017, he joined the China University of Mining and Technology, (CUMTB), Beijing, China. After a postdoctoral research phase with the GFZ German Research Centre for Geosciences, Potsdam, Germany, from 2018 to 2019, he returned to CUMTB, where he does research and lectures in monitoring and modeling of ground surface deformations related to mining activities, groundwater extraction, oil exploitation, and CO_2 injection, etc.

Wei Zhan received the Ph.D. degree in geodesy from Wuhan University, Wuhan, China.

He is currently an Associate Professor with the First Monitoring and Application Center, China Earthquake Administration, China. His research focused on geodetic data and their accuracy analysis. His research interests include seasonal crustal deformation analysis based on GPS, GRACE, and mass loading model.

Bowen Jin received the master's degree in geodesy from the China University of Geosciences, Wuhan, China, in 2015.

He is currently an Engineer with the National Marine Data and Information Service (NMDIS), Tianjin, China. He is mainly responsible for the processing and analysis of continuous GNSS data and tide gauge records, and assessment of the impact of sea level changes along coastal region.

Mahdi Motagh was born in Tehran, Iran, in 1975. He received the B.Sc. degree in surveying engineering and the M.Sc. degree in geodesy from the University of Tehran, Tehran, Iran, in 1998 and 2002, respectively, and the Ph.D. degree in earth sciences from the University of Potsdam, Potsdam, Germany, in 2007.

As of 2007, he was a Postdoctoral Scientist with GFZ German Research Center for Geosciences, Potsdam, Germany, where he became a Permanent Research Staff, in 2011. In 2017, he became a Professor for radar remote sensing with Leibniz University Hannover in Germany. He also has a Guest Professorship with Wuhan University in China.

Yubin Xu received the Ph.D. degree in photogrammetry and remote sensing from the School of Earth and Space Sciences, Peking University, Beijing, China, in 2014.

In 2014, he joined China Academy of Civil Aviation Science and Technology, Tianjin, China. He is now focusing on aerodrome clearance management on the basis of satellite remote sensing, aerodrome deformation, and eTOD, etc.